CHEMISTRY OF MATERIALS

Open Access

This article is licensed under CC-BY 4.0

pubs.acs.org/cm

Article

Structural, Electronic, and Magnetic Curiosities of an Unprecedented Chromate (II)

Published as part of Chemistry of Materials special issue "In Memory of Prof. Francis DiSalvo".

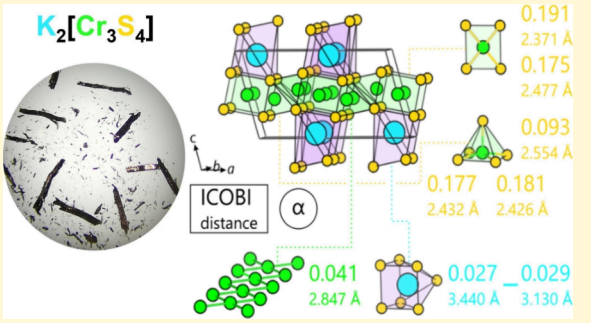
M. Reza Ghazanfari, Simon Steinberg, Götz Schuck, Konrad Siemensmeyer, Mirko Tallu, Johannes C. Vrijmoed, Stefanie Dehnen, and Günther Thiele*

Cite This: *Chem. Mater.* 2024, 36, 9658–9665

Read Online

ACCESS | Metrics & More | Article Recommendations | Supporting Information

ABSTRACT: The ternary sulfido chromate (II), $K_2[Cr_3S_4]$, was synthesized through a straightforward solid-state method as the first alkali metal chalcogenido chromate with the formal oxidation state +2, which was verified by X-ray absorption spectroscopy. Single-crystal diffraction analysis reveals the chromium ions to be coordinated by sulfur in two geometric arrangements: square planar and square pyramidal. Both environments are unusual for transition metal complexes with a d^4 electron configuration. Structural distortions from the ideal arrangement are present in both coordination environments. Measurement of the magnetic moment indicates a value of 3.60 μB per chromium ion, which appears at first glance to contradict the standard ligand field theory. Quantum chemical calculations suggest high-spin states for both coordination geometries with a spin delocalization due to Cr−Cr interactions, leading to an intermediate-spin state with magnetic moment values very close to the experimental results, and attributing the structural distortions as the first example of the Jahn−Teller active d^4 system with nonoctahedral coordination geometries. The optical, dielectric, and impedance measurement results indicate the potential as a synergic insulator, capacitor, and high-dielectric-constant material.

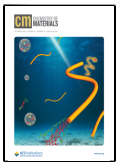


INTRODUCTION

Inorganic metalate salts of 3*d* transition metals are a well-known class of solid-state materials, including unique candidates for electronic[1] and spintronic[2] applications. These materials can be obtained incorporating various elemental constituents at different ratios, yielding a large number of different structure types, which allow the design of chemical and physical properties accordingly.[3,4] Most of the literature-known chromate salts are based on chalcogenido and halogenido chromate anions. The well-known oxido chromate (VI) anion, $[CrO_4]^{2-}$, and oxido dichromate (VI) anion, $[Cr_2O_7]^{2-}$, can be found in many laboratories, as well as be employed for corrosion protection coating and as oxidizing agents.[5,6] Although chromium ions, in general, can obtain several formal oxidation states, ranging from −4 to +6, the most common ones are +2, + 3, and +6.[7] Chromate (VI) compounds usually have less stability compared to chromates (III). Compounds containing chromium in the formal oxidation state +2 are mainly unstable and comparably uncommon as they are prone to rapid oxidation or decomposition to chromium(III), especially when exposed to air.[8] The toxicity of the chromium-containing compounds is reduced by decreasing the oxidation states. While the chromates (VI) are very toxic and carcinogenic, chromates (III) are typically nontoxic.[9]

There are several known oxido- and chalcogenido chromates (III): $K[CrO_2]$,[10] $Na[CrO_2]$,[11] $K[Cr_5S_8]$,[12] $Rb[Cr_5S_8]$,[12] $Cs[Cr_5S_8]$,[12] $Li[CrS_2]$,[13] $Rb[Cr_5Se_8]$,[14] and $K[CrSe_2]$.[15] In contrast, chromate (II) compounds are very rare, and the only literature-reported ternary alkali metal chromates are halogenido chromates: $Rb[CrCl_3]$,[16] $Cs[CrCl_3]$,[16] $Rb[CrI_3]$,[17] $Rb[CrBr_3]$,[18] $Li_2[CrCl_4]$,[19] $Na[CrF_3]$,[20] and $K[CrF_3]$.[21] The chromium ions in all of these compounds, similar to the chromates (III), are octahedrally coordinated by halogens and typically crystallize in the double perovskite structure type.[22] These compounds, containing octahedral chromium(II), are well-known for exhibiting the Jahn−Teller effect, which is a structural distortion resulting from an asymmetric electron configuration.[19−21] The energetic degeneration of the e_g representation (ideal high-spin case) is lost, resulting in

Received: June 25, 2024
Revised: September 16, 2024
Accepted: September 18, 2024
Published: September 30, 2024



Downloaded via HELMHOLTZ ZENTRUM BERLIN on December 4, 2024 at 16:19:33 (UTC).
See https://pubs.acs.org/sharingguidelines for options on how to legitimately share published articles.

© 2024 The Authors. Published by American Chemical Society

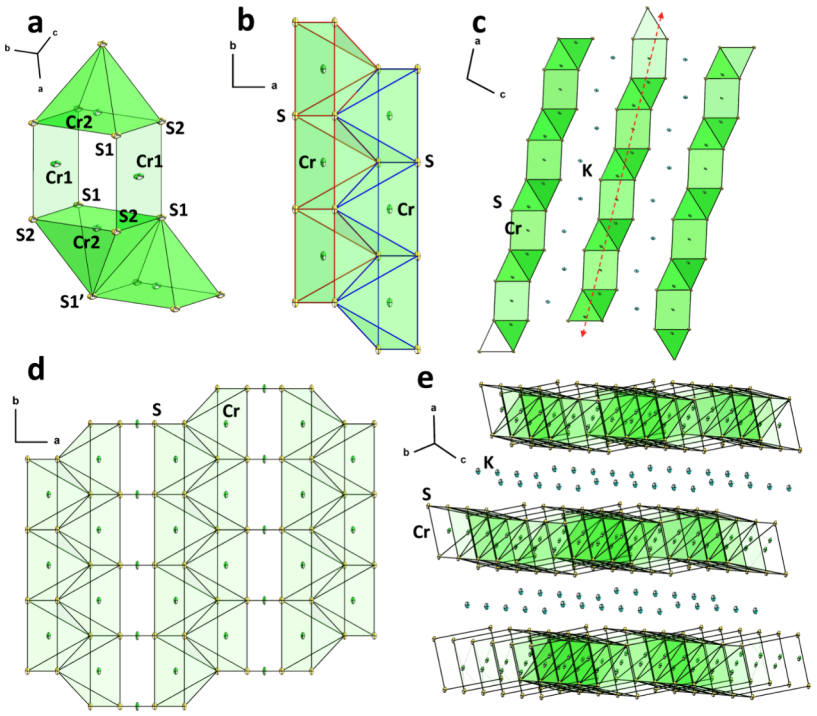


Figure 1. Excerpts of the crystal structure of **1**. (a) Depicted along the (111) direction, indicating the edge and/or corner sharing square planar and square pyramidal polyhedra. (b) The edge-sharing square pyramidal polyhedra, creating antiparallel strands along the *b*-axis. (c) Depicted along the *b* axis, displaying anionic layers propagating in the *ab* plane (red arrow line depicts interconnection of strands). (d) Depicted along the *c* axis, displaying the anionic substructure. (e) The anionic layers and layers of potassium ions positioned in between.

different levels of distortion in the crystal structure as well as variations in the electronic and magnetic properties.[20,21] To the best of our knowledge, potential impacts of the different coordination environments of chromates (II) are still unknown, as neither nonhalide chromate (II) of alkali metals nor nonoctahedrally coordinated chromate (II) salts are reported so far. One of the unique aspects of chromium chemistry lies in its diverse coordination environments, which can significantly influence the physical properties of its compounds. In particular, chromium(II) tends to exhibit a range of coordination geometries, including octahedral, tetrahedral, and square planar, depending on the ligands and overall structure of the compound.[5,7,16] The coordination environment directly affects the electronic structure of chromium, leading to variations in properties such as magnetism, electronic band structure, and optical behavior.[20,21] This is especially relevant in compounds where nonhalide ligands, such as chalcogenides, are involved, as they can introduce new bonding interactions and distortions that are distinct from those observed in more common halide chromates. Thus, the exploration of chalcogenido chromates (II), such as $K_2[Cr_3S_4]$ (**1**), opens up new avenues for understanding how these coordination environments affect the overall behavior of the material.

Based on our previous investigations on sulfido metalates of the transition metals,[23] we were interested to expand these investigations to the electron poorer transition metals, i.e., chromium. In this work, we report the synthesis of the first alkali metal chalcogenido chromate (II), **1**, in a multigram scale through a straightforward and time-efficient synthetic method. The structural investigations and further evaluations of the magnetic, electronic, and optical properties as well as quantum chemical calculations were conducted to reveal their correlations.

RESULTS AND DISCUSSION

Synthesis and Structural Properties. **1** was synthesized through a straightforward solid-state reaction by fusion of an intimate mixture of K_2S, Cr, and S with the stoichiometric ratio of 1:3:3 at a temperature of around 1273 K for approximately 10 min under a constant flow of argon, according to the following reaction equation:

$$K_2S + 3Cr + 3S \xrightarrow[\approx 10\text{min}]{\approx 1273\text{K}} K_2[Cr_3S_4] \quad (1)$$

The reaction yielded 15.36 g (93% yield) of **1** as a metallic shiny powder of dark gray color. The reaction can be scaled up by using larger reaction containers. The mass loss originates from a residual material at the wall of the container. Single crystals of **1**, obtained via a solvothermal post-synthetic treatment in pyridine at 423 K for 48 h, indicate a needle-shaped morphology and dark gray color. **1** crystallizes in the monoclinic space group *C*2/*m* according to the single-crystal X-ray diffraction (SC-XRD) results. Information about the refinement procedure and structural parameters are available in the Supporting Information. Figure 1 displays an excerpt of the crystal structure. The Cr ions are located in two coordination geometries: square planar (Cr1) and square pyramidal (Cr2; Figure 1a). In the square planar and square pyramidal polyhedra the chromium ions are coordinated by four and five sulfur ions, respectively. The square pyramidal polyhedra are connected to each other by edge-sharing to yield two antiparallel strands (Figure 1b). These strands are interconnected via the square planar polyhedra by additional edge-sharing along the crystallographic *a*-axis (red arrow line, Figure

https://doi.org/10.1021/acs.chemmater.4c01764
Chem. Mater. 2024, 36, 9658−9665

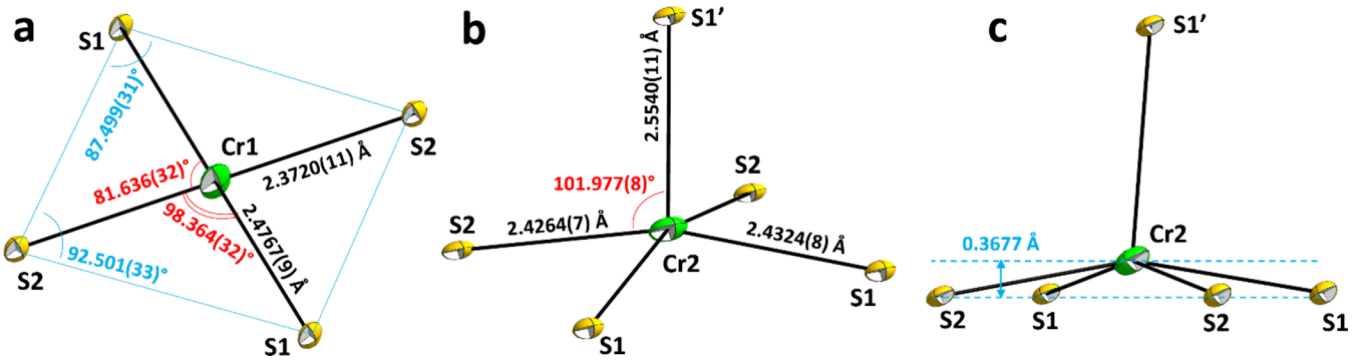


Figure 2. ORTEP diagram of the chromium coordination in **1**, displaying the bond lengths and angles in (a) the square planar coordination geometry of $[CrS_4]^{6-}$, (b, c) the square pyramidal coordination geometry of $[CrS_5]^{8-}$. Deviations in the bond lengths and angles in both square planar and square pyramidal environments indicate slight distortions in the crystal structure compared to the ideal geometries.

1c). This interconnection of pyramidal and planar polyhedra creates overall two-dimensionally extended anionic layers (Figure 1d,e). Within these anionic layers, there are two square pyramidal polyhedra of $[CrS_5]^{8-}$ per square planar polyhedron of $[CrS_4]^{6-}$. Within the square planar polyhedra (Figure 2a), the chromium−sulfur bond lengths are 2.3720(11) Å for Cr1−S1 and 2.4767(9) Å for Cr1−S2, indicating a small distortion from the ideal square planar geometry. The squares are slightly distorted to a rhombus shape with corner angles of 92.501(33) and 87.499(31)°, while the bond angles of adjacent S1−Cr1−S2 and S2−Cr1−S1 are 81.636(32) and 98.364(32)°, respectively. Within the square pyramidal polyhedra (Figure 2b,c), the chromium−sulfur bond lengths are 2.4264(7) Å for Cr2−S1 and 2.4324(8) Å for Cr2−S2, in the basal planes, while the chromium ions are positioned out of the basal planes (0.3677 Å above the plane, see Figure 2c) with the angle of S2−Cr2−S1′ of 101.977(8)°. The corner angles of the square basal planes are 90.000(14)°, indicating an ideal square shape without distortion. The Cr2−S1′ bond lengths are 2.5540(11) Å. The polyhedra are slightly distorted by elongation toward the apical sulfide ligand. Potassium ions are located in between such $[Cr_3S_4]$-layers with the closest sulfur neighbors forming face-sharing distorted octahedra. The coordination geometries of square planar and square pyramidal are more common for electron-rich 3*d*-transition metals such as Co and Cu,[24,25] while **1** is the first $3d^4$ system indicating these coordination environments. Based on standard ligand field theory (*vide infra*), in both the low-spin and the high-spin states, the electron configurations are symmetric, preventing Jahn−Teller effects as an origin of the experimentally observed distortions.

The phase purity of **1** was evaluated by using powder X-ray diffraction (P-XRD). The Rietveld refinement (Figure S1) shows the purity of **1** of around 98 wt % with a negligible amount (less than 3 wt %) of literature-known $KCrS_2$ as a side product. Due to the considerable impact of preferential orientations (needle-shaped crystals), this quantification is not fully reliable and can only serve as an estimate. The Rietveld refinement of **1** indicates a crystallinity degree of 85 ± 2% and an average crystallite size of 557 ± 16 nm. The elemental ratios in **1** were analyzed based on energy-dispersive X-ray spectroscopy (EDX), verifying the stoichiometric ratio of 2:3:4 for K:Cr:S (Figure S2). More details of the P-XRD and EDX measurements are provided in the Supporting Information.

The thermal stability profile of **1** was evaluated by thermogravimetry coupled with differential scanning calorimetry (TG/DSC) measurements. No observable phase transformation or mass loss occurred up to 1000 K (upper limit of the measurement). According to the obtained sum formula of **1**, based on the SC-XRD and EDX results, the nominal average oxidation state of Cr ions is +2, when considering the oxidation states of potassium and sulfur ions equal to +1 and −2, respectively. To experimentally prove the oxidation state of chromium ions in **1**, the shifts of the X-ray absorption edges were investigated in the X-ray absorption near-edge structure spectroscopy (XANES) region.

Figure 3a shows the XANES region of the XAS spectra of **1** in comparison to the measured spectra of elemental

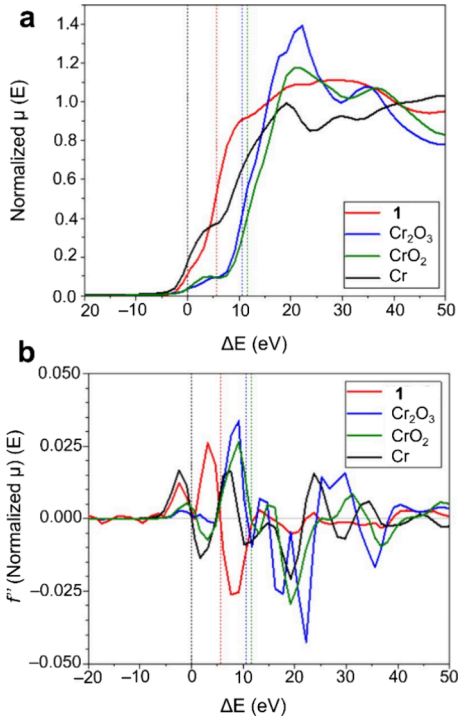


Figure 3. X-ray absorption near-edge structure spectroscopy (XANES) of (a) normalized XAS spectra (energy calibrated) of the chromium K-edge of **1** and reference materials, and (b) the second derivative of normalized XAS spectra of **1** and reference materials: chromium metal foil (black), Cr_2O_3 (blue), CrO_2 (green), and **1** (red).

https://doi.org/10.1021/acs.chemmater.4c01764
Chem. Mater. 2024, 36, 9658−9665

chromium(0), chromium(III) oxide, Cr_2O_3, and chromium-(IV) oxide, CrO_2, as reference materials. E_0 was determined after energy calibration for CrO_2, Cr_2O_3, and **1** from the zero crossing of the respective main feature[26] of the second derivative of the XAS spectra (Figure 3b). Further information about the preparative procedure and details on the measurements can be found in the Supporting Information.

For the two reference materials Cr_2O_3 and CrO_2, the energy shifts, ΔE, are 10.6 and 11.6 eV, respectively, which were experimentally determined relative to the energy position of the elemental chromium K-edge (5989.0 eV). To determine the oxidation state of chromium ions in **1**, these values can be compared with the value of ΔE (**1**) = 5.6 eV, experimentally determined for **1**, as well as the reported values in the literature for various chromium compounds.[26]

The ΔE value of **1** is in between the ΔE values of elemental chromium and Cr_2O_3, suggesting the oxidation state of chromium ions in **1** being between 0 and +3. The energy positions of the measured reference materials (Figure S3) can be described with a linear function that shows that for **1**, an oxidation state of +2 tends to be in the slightly upper range of the energy position of ΔE (**1**), in agreement with the literature-reported prediction of the energy shifts for compounds with different chromium oxidation states.[26]

Magnetic Properties. Figure 4a shows the field-dependent magnetization hysteresis curves of **1** by applying a magnetic field up to 5.00 T at temperatures of 4, 30, and 300 K. At low temperatures, the curves illustrate linear trends with the saturation region beginning at applied magnetic fields higher than 2.00 T. At high temperatures (300 K), the magnetization curve is fully linear with very low magnetic susceptibilities and without any saturation, indicating a paramagnetic structure of **1**. The temperature-dependent magnetization plots, including field cooling (FC) and zero field cooling (ZFC) are shown in Figure 4b. By increasing the temperature, the magnetization values in both FC and ZFC curves are increased from around 10−50 K and then sharply decreased to a plateau level up to 370 K (the measurement upper limit), indicating an antiferromagnetic (AFM) structure. The initial decrease of magnetization values in the range of 4−10 K, often termed a Curie tail,[27] might be attributed to the minor effects of $KCrS_2$ impurity or other by P-XRD undetectable impurities. Further discussions on the potential effects of impurities on the magnetic properties are provided in the Supporting Information. The inverse magnetic susceptibility (Figure S7) can be fitted according to the Curie−Weiss law on the FC curve at temperatures higher than 100 K, suggesting a Néel temperature of around 100 K. The effective magnetic moment, calculated from the inverse susceptibility curve, is 3.60 μB per chromium ion. This value is lower than expectations from the standard ligand field theory for d^4 systems. The high-spin electron configurations in both square planar and square pyramidal geometries would predict 4.89 μB per chromium ion. According to standard ligand field theory, the square planar and square pyramidal geometries of **1** provide two different orbital splittings (Figure 4b-inset). At first glance, this appears contradicting and suggests an uncommon magnetic behavior of chromium ions in **1**. The low-spin and high-spin states in both coordination geometries would be expected to give magnetic moments of around 1.86 and 4.89 μB per chromium ion, respectively, which contradict the experimentally obtained value (3.60 μB). In the literature, such a contradiction between experimentally measured magnetic

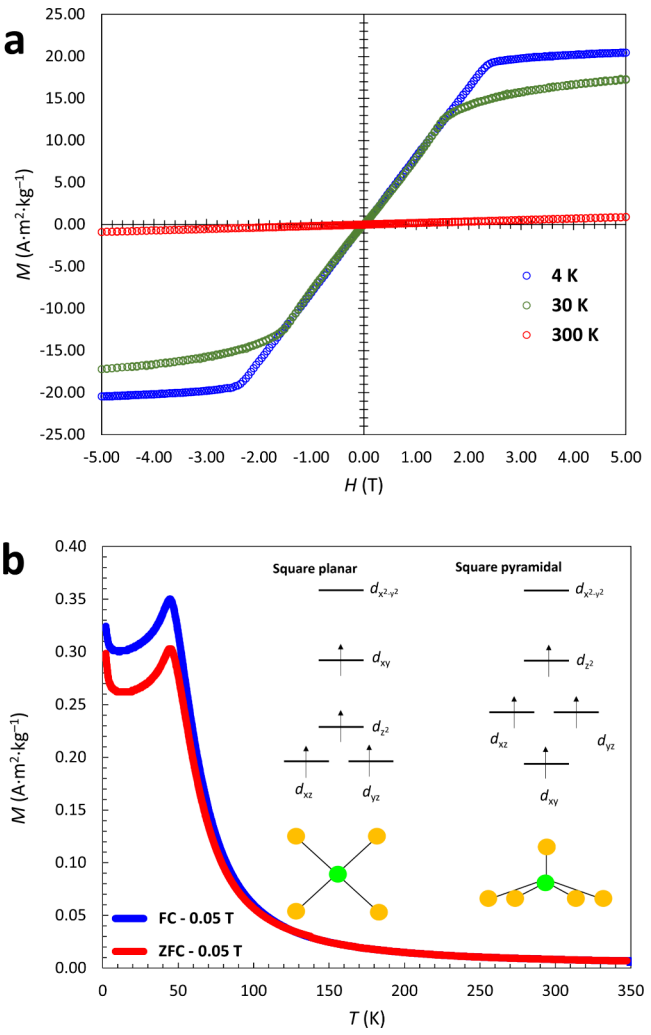


Figure 4. (a) Field-dependent magnetization curves for **1** at different temperatures as a function of the external applied field up to 5.00 T. (b) Zero field cooling (ZFC) and field cooling (FC) plots of **1** as a function of measurement temperature under an applied field of 0.05 T. (b-inset) Molecular orbital diagrams according to standard ligand field splitting for d^4 square planar coordination geometry with a high-spin state (left side) and the square pyramidal coordination geometry when the center metal ion is out of the basal coordinating plane, showing a high-spin state (right side).

moments and the calculated ones is reported for Y_2CrS_4.[28,29] The oxidation state of chromium ions in Y_2CrS_4 is given as 2+, with an octahedral coordination of chromium ions. In 2007, Tezuka et al. reported the effective magnetic moment of 3.27 μB for chromium ions in Y_2CrS_4 according to the powder neutron diffraction results measured at 10 K.[28] A few years later, Liu et al. reported the magnetic moments of 3.53 μB for chromium ions in Y_2CrS_4, experimentally measured according to the magnetic susceptibility curve in the range of 150−300 K.[29] In both studies, a Néel temperature of around 65 K is reported. Additionally, signs of ferromagnetic components at temperatures lower than the Néel temperature are mentioned, which is in agreement with the observed Curie tail in the present study. However, within the studies on Y_2CrS_4, no explanations about the differences between the measurements results and theory are given.

Density Functional Theory Calculations. To investigate the apparent discrepancy of the magnetic results with the

https://doi.org/10.1021/acs.chemmater.4c01764
Chem. Mater. 2024, 36, 9658−9665

ligand field theory as well as the unexpected structural distortions, the electronic structure of **1** was explored using density functional theory (DFT)-based means (see the Supporting Information). In the framework of these computations, the structure models were also optimized so that the overall geometry was kept in the final circles of the calculations. The DFT results indicate an indirect band gap with an energy of 1.52 eV (Figure 5a) at an optimized U-value

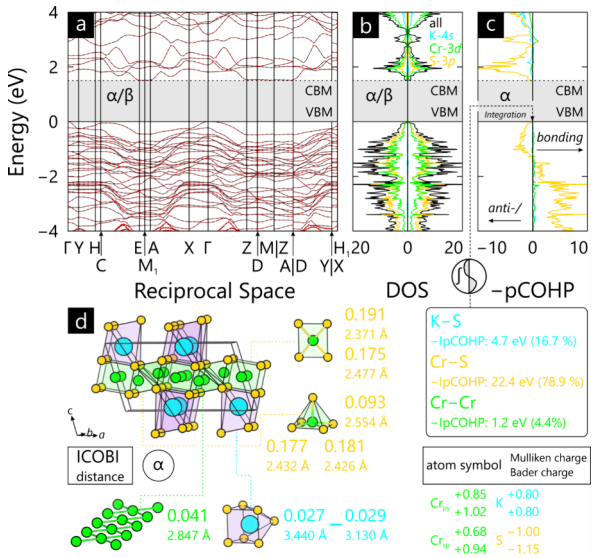


Figure 5. (a) Spin-polarized electronic band structure and (b) densities-of-states (DOS) curves of **1**. (c) The projected crystal orbital Hamilton populations (pCOHP) and (d) integrated crystal orbital bond indices (ICOBI), which have been provided for one of the spin channels.

of 3.7 to match the experimental optical band gap (Figure S4). The computed densities-of-states (DOS) (Figure 5b) display the dominant contributions of Cr-*d* and S-*p* in both conductive and valence bands. Calculations were carried out based on the different starting models of low-, intermediate-, and high-spin states by inputting the initial magnetic moments of 0, 2.8, and 3.7 (both for intermediate-spin), and 4.9 μB (obtained according to standard ligand field theory), respectively. In all cases, the final values of computed magnetic moments were around 3.64 μB, which is in a good agreement with the experimentally obtained magnetic moment (3.60 μB) and confirms a deviation from the pure high-spin states.

A closer inspection of the electronic situation indicates Cr−Cr interactions and partial delocalization of the spin states. The experimentally obtained distance between Cr1 and Cr2 is around 2.8468(2) Å. Such an interaction explains the structural distortions in the coordination environment of chromium ions, as well as the unexpected magnetic moment of **1**. The Cr−Cr interactions might cause a partial delocalization in the spin states in the square planar and square pyramidal molecular orbitals. The delocalized spin state systems of the square planar environments can lead to asymmetric electron configurations and thus Jahn−Teller-like distortion. The above-mentioned spin state delocalization changes the final magnetic moments, while the calculated average magnetic moment for these molecular orbitals is around 3.87 μB, which is comparable to the experimental value of 3.60 μB. Further experimental analysis, including neutron powder diffraction, is planned.

Electrical Properties. Motivated by high k values and outstanding electrical conductivities found for metalate salts with 2D extended anionic sublattices,[23] the dielectric and impedance properties of **1** were investigated. The dielectric constant of **1** at a frequency of 1 kHz is around 437, which is remarkably high compared to the reference material SiO_2 (k = 3.6−3.9).[30,31] The electrical resistivity as well as dielectric constant and loss values of **1** decrease by increasing the frequency in the range of 0.10−100 kHz (Figure S5). The results of the complex impedance spectroscopy of **1** (Figure S6) indicate a semicircular arc with bulk resistivity and ionic conductivity values of around 28 kΩ and 66 $\mu S \cdot cm^{-1}$, respectively. The semicircular trend of the Nyquist plot indicates the ionic nature of the conductivity as a dominant mechanism of the electrical conductivity. Due to the layered structure of **1**, potassium ion migration within the cationic layers, between anionic layers, could be considered as the main ionic conducting process. Further details of the electrical measurements and results are available in the Supporting Information.

CONCLUSIONS

In the current work, the first alkali metal chalcogenido chromate, $K_2[Cr_3S_4]$, with chromium ions in the formal oxidation state of +2 was obtained through a large-scale synthetic method. $K_2[Cr_3S_4]$ is the first metalate with d^4 configuration of the center metal ion with square planar and square pyramidal coordination environment including a slight structural distortion. Partially delocalized intermediate-spin states explain the structural distortion as well as the unexpected magnetic moments. This work presents a novel compound with unexpected structural distortions, coordination environments, and magnetic properties, as well as the first electrical characteristics of a nonhalide chromate (II).

EXPERIMENTAL SECTION

Materials and Synthetic Approaches. The starting materials including potassium (Acros Organics, 98%), chromium (Merck, 99.5%), and sulfur (abcr, 99%) were purchased commercially and utilized without further purifications. As a binary starting material, K_2S was synthesized by reacting the stoichiometric ratio of potassium (2 equiv, 0.513 mol, 20.26 g) and sulfur (1 equiv, 0.257 mol, 8.30 g) in liquid ammonia at temperature of 235 K, according to the literature.[32] Before using, the purity of the as-synthesized product is evaluated and confirmed using the P-XRD technique. Due to the sensitivity of some starting materials as well as products to air/moisture exposure, all preparation and manipulation steps were conducted inside an argon-filled glovebox and/or under argon flow through the Schlenk-line technique.

To synthesize **1**, the stoichiometric ratio of K_2S (1 equiv, 0.047 mol, 5.270 g), Cr (3 equiv, 0.136 mol, 7.073 g), and S (3 equiv, 0.135 mol, 4.362 g) was homogeneously mixed, transferred to a silica glass ampule, and heated up to around 1273 K for 10 min under constant flow of argon, using an oxygen−methane flame torch. After cooling the ampule down to room temperature, it was transferred to a glovebox, carefully broken, and the crude product was manually selected and ground to a fine powder. The single crystals of **1** were obtained from a solvothermal treatment by placing around 125 mg of fine powder and 2 mL of pyridine into a 10 mL glass vial with a designed pressure release cap (>3 bar) and heating at 423 K for 48 h.

Characterization Techniques. To determine the crystal structure of **1**, the single crystals were isolated and picked under a light microscope and mounted in Paraton oil. The picked crystals were measured using a Bruker D8 Venture diffractometer with Mo−K_α radiation (λ = 0.71073 Å) at 100 K. The crystal structure was

https://doi.org/10.1021/acs.chemmater.4c01764
Chem. Mater. 2024, 36, 9658−9665

solved and refined in Olex2[33] using ShelXT[34] and ShelXL,[35] respectively. To present the depictions of the crystal structure, it was depicted using DIAMOND4.5.2.[36] The phase purities of the starting materials as well as **1**, finely ground powders were investigated using a Malvern Panalytical Empyrean using Cu−K_α radiation (λ = 1.54184 Å) at 293 K. The samples were prepared by placing approximately 50 mg powder on a self-printed PLA sample-holder according to the reported protocol.[37] The P-XRD results were refined based on the Rietveld structure refinement[38] technique using GSAS II[39] to extract the crystallographic parameters such as crystallinity degree and crystallite size. Additionally, an evaluation of the elemental ratio of **1** was conducted using energy-dispersive EDX. More details of the SC-XRD, P-XRD, and EDX measurements and results are provided in the Supporting Information.

To carry out the XANES measurements, chromium K-edge (5989.0 eV) XAS was measured on the KMC-2 beamline[40] at BESSY II synchrotron at Helmholtz-Zentrum Berlin. This beamline operates a graded SiGe monochromator constructed of two independent crystals (energy resolution of $E/\Delta E$ = 4000). The beam intensity at KMC-2 is stabilized to an accuracy of 0.3%. The Athena software from the Demeter 0.9.26 software suite[41] was used for normalization and energy calibration. For the energy calibration, a Cr metal foil was measured simultaneously as a reference material in each case of XAS measurements. For all samples, XAS measurements were conducted in transmission mode. To prepare sample for the XANES measurements, fine powder of **1** and the reference materials were brushed onto a Kapton tape. For **1**, the sample preparation was done in a glovebox, and the Kapton tape with the sample was then subsequently sealed in an airtight sample container in the glovebox.

The UV−visible spectroscopy measurements were conducted by placing around 5 mg of fine powder into a Praying Mantis accessory by recording the optical reflection spectra using a Varian Cary 5000 UV/vis/NIR spectrometer in the wavelength range of 200−1400 nm. The plotted results of the UV−vis measurements are available in the Supporting Information. Magnetic measurements were carried out by preparing samples of around 15−20 mg of fine powder into a polyethylene capsule and then transferred to a superconducting quantum interference device magnetometer (SQUID, MPMS3-7T Quantum Design). The measurements were done at different temperatures of 4, 30, and 300 K under an applied field of up to 5.00 T. The FC and ZFC measurements were conducted under an applied field of 0.05 T.

To measure the electrical resistivity, dielectric, and impedance properties of **1**, approximately 400 mg of fine powder was placed in a stainless-steel mold with the diameter of 13 mm and pressed as pellets by applying pressure up to 80 kN·cm^{-1} using a uniaxial hydraulic press. The pressed pellets were sintered at a temperature of 973 K for 12 h under an argon atmosphere, covered on both sides by silver paste (abcr, sheet resistivity <3.8 × 10^{-3} Ωcm^{-1}, for the layer thickness of 3.8 × 10^{-4} cm), as electrodes, and then dried at 373 K for 60 min. The dielectric properties of pellets were measured at room temperature and in the frequency range of 0.10−100 kHz using an LCR meter (East Tester, ET4410), while the impedance properties were measured at the same temperature and in the frequency range 100 mHz to 100 MHz using an electrochemical impedance analyzer (EIS, BioLogic MTZ-35). Analyzing and simulating the complex impedance plots were carried out utilizing ZSimpWin program.[42] The corresponding ionic conductivity values were calculated based on the Nyquist equation.[43]

■ ASSOCIATED CONTENT

Data Availability Statement

All data supporting the findings of this study are provided in the main text of the article and the Supporting Information file. Raw data sets can be obtained from the corresponding author on request. Crystal structure data of **1** are provided as a CIF file. Any additional data required will be made available upon request.

Supporting Information

The Supporting Information is available free of charge at https://pubs.acs.org/doi/10.1021/acs.chemmater.4c01764.

Details of crystal structure refinement and crystal data, P-XRD results and Rietveld refinement, EDX results, XANES results, magnetometry results, sintering process of samples, dielectric and impedance measurements, and the Tauc plot of UV−vis spectroscopy of the compound (PDF)

■ AUTHOR INFORMATION

Corresponding Author

Günther Thiele − *Fachbereich Biologie, Chemie, Pharmazie, Freie Universität Berlin, Berlin 14195, Germany; Institut für Anorganische und Analytische Chemie, Albert-Ludwigs-Universität Freiburg, Freiburg 79104, Germany;* orcid.org/0000-0003-2935-9335; Email: guenther.thiele@fu-berlin.de

Authors

M. Reza Ghazanfari − *Fachbereich Biologie, Chemie, Pharmazie, Freie Universität Berlin, Berlin 14195, Germany*

Simon Steinberg − *Institut für Anorganische Chemie, RWTH Aachen, Aachen 52074, Germany*

Götz Schuck − *Helmholtz-Zentrum Berlin für Materialien und Energie, Berlin 14109, Germany;* orcid.org/0000-0002-0624-2719

Konrad Siemensmeyer − *Helmholtz-Zentrum Berlin für Materialien und Energie, Berlin 14109, Germany*

Mirko Tallu − *Institute of Nanotechnology (INT), Karlsruhe Institute of Technology (KIT), Karlsruhe 76131, Germany*

Johannes C. Vrijmoed − *Fachbereich Geowissenschaften, Freie Universität Berlin, Berlin 12249, Germany*

Stefanie Dehnen − *Institute of Nanotechnology (INT), Karlsruhe Institute of Technology (KIT), Karlsruhe 76131, Germany;* orcid.org/0000-0002-1325-9228

Complete contact information is available at: https://pubs.acs.org/10.1021/acs.chemmater.4c01764

Author Contributions

Conceptualization: M.R.G. and G.T.; project administration: M.R.G. and G.T.; writing initial draft: M.R.G.; synthesis and formal analysis: M.R.G.; DFT calculations, analysis, and visualization: S.S.; XANES measurements, analysis, and visualization: G.S; investigation of magnetic properties: K.S.; conducting of UV−vis spectroscopy: M.T.; resources for EDX measurements: J.C.V.; resources for UV−vis spectroscopy measurements: S.D.; resources for synthesis, impedance and dielectric properties: G.T.; funding acquisition: G.T.; review and editing: M.R.G. and G.T.; supervision: G.T. All authors have given approval to the final version of the manuscript.

Notes

The authors declare no competing financial interest.

■ ACKNOWLEDGMENTS

We thank the Verband der Chemischen Industrie e.V. for a Liebig scholarship, the Volkswagen Stiftung within the framework of an "Experiment!" funding, the German-American Fulbright Commission for a Fulbright-Cottrell Award. Helmholtz-Zentrum Berlin (HZB) is acknowledged for supporting the allocation of synchrotron radiation beamtime at KMC-2 (BESSY II). Core facility BioSupraMol is acknowl-

edged for X-ray diffraction time. We thank Alaa Alter, Friederike Fuß, Islam Ramadan, and Asad Malik for their supports in the reproduction of the synthesis, UV−visible spectroscopy, SC-XRD, and P-XRD measurements, respectively. We thank Dr. Karel Prokes and the Quantum Materials Core Lab facilities at Helmholtz-Zentrum Berlin (HZB) for the magnetic measurements.

REFERENCES

(1) Ohkubo, I.; Mori, T. Rational Design of 3d Transition-Metal Compounds for Thermoelectric Properties by Using Periodic Trends in Electron-Correlation Modulation. *J. Am. Chem. Soc.* **2022**, *144*, 3590−3602.
(2) Zibouche, N.; Kuc, A.; Musfeldt, J.; Heine, T. Transition-Metal Dichalcogenides for Spintronic Applications. *Ann. Phys. (Berl.)* **2014**, *526*, 395−401.
(3) Friedländer, S.; Liu, J.; Addicoat, M.; Petkov, P.; Vankova, N.; Rüger, R.; Kuc, A.; Guo, W.; Zhou, W.; Lukose, B.; Wang, Z.; Weidler, P. G.; Pöppl, A.; Ziese, M.; Heine, T.; Wöll, C. Linear Chains of Magnetic Ions Stacked with Variable Distance: Ferromagnetic Ordering with a Curie Temperature above 20 K. *Angew. Chem., Int. Ed.* **2016**, *55*, 12683−12687.
(4) Herrmann, W. A. Multiple Bonds between Transition Metals and "Bare" Main Group Elements: Links between Inorganic Solid State Chemistry and Organometallic Chemistry. *Angew. Chem., Int. Ed.* **1986**, *25*, 56−76.
(5) Arévalo-López, A. M.; Alario-Franco, M. A. Reliable Method for Determining the Oxidation State in Chromium Oxides. *Inorg. Chem.* **2009**, *48*, 11843−11846.
(6) Brett, C. M. A.; Gomes, I. A.; Martins, P. The Electrochemical Behavior and Corrosion of Aluminum in Chloride Media. *Corros. Sci.* **1994**, *36*, 915−923.
(7) Vincent, J. B. *The Bioinorganic Chemistry of Chromium*; John Wiley & Sons, Ltd: Chichester, UK, 2013 ISBN 978−0-470−66482−7.
(8) Holleman, A. F.; Wiberg, E.; Wiberg, N. *Lehrbuch der Anorganischen Chemie*, 91−100 ed. De Gruyter: Germany, 1985 ISBN 978−3-11−007511−3.
(9) Banci, L. *Metallomics and Cellular Metal Homeostasis*; Springer Dordrecht 2013
(10) Scheld, W.; Hoppe, R. Über den α-NaFeO2-Typ: Zur Kenntnis von NaCrO2 und KCrO2. *Z. Anorg. Allg. Chem.* **1989**, *568*, 151−156.
(11) Quak, D.-H.; Sarif, M.; Opitz, P.; Lange, M.; Jegel, O.; Pham, D. H.; Koziol, M.; Prädel, L.; Mondeshki, M.; Tahir, M. N.; Tremel, W. Generalized synthesis of $NaCrO_2$ particles for high-rate sodium ion batteries prepared by microfluidic synthesis in segmented flow. *Dalton Trans.* **2022**, *51*, 10466−10474.
(12) Huster, J. Darstellung und Kristallstruktur der Alkalithiochromate (III), ACr_5S_8 (A ≙ Cs, Rb und K). *Z. Anorg. Allg. Chem.* **1978**, *447*, 89−96.
(13) White, J. G.; Pinch, H. L. The Crystal Structure of Lithium Thiochromite, $LiCrS_2$. *Inorg. Chem.* **1970**, *9*, 2581−2583.
(14) Bronger, W.; Herudek, C.; Huster, J.; Schmitz, D. Neue Alkalimetallchromchalkogenide und ihre Struktursystematik. *Z. Anorg. Allg. Chem.* **1993**, *619*, 243−252.
(15) Song, X.; Schnieder, S. N.; Cheng, G.; Khoury, J. F.; Jovanovic, M.; Yao, N.; Schoop, L. M. Kinetics and Evolution of Magnetism in Soft-Chemical Synthesis of $CrSe_2$ from $KCrSe_2$. *Chem. Mater.* **2021**, *33*, 8070−8078.
(16) Crama, W. J.; Maaskant, W. J. A.; Verschoor, G. C. The Cooperative Jahn-Teller Distorted Structures of Rubidium Chromium(II) Trichloride and Caesium Chromium(II) Trichloride. *Acta. Crystallogr. B. Struct.* **1978**, *34*, 1973−1974.
(17) Zandbergen, H. W.; Ijdo, D. J. W. Neutron Powder Diffraction on $RbCrI_3$ and Magnetic Measurements on $RbCrI_3$ and $CsCrI_3$. *J. Solid State Chem.* **1981**, *38*, 199−210.
(18) Griesemer, S. D.; Ward, L.; Wolverton, C. High-throughput Crystal Structure Solution using Prototypes. *Phys. Rev. Mater.* **2021**, *5*, No. 105003.
(19) Lutz, H. D.; Schneider, M.; Wickel, C. Neutron Powder Diffraction on Monoclinic Li_2CrCl_4. *Z. Kristallogr. - Cryst. Mater.* **1996**, *211*, 8−12.
(20) Bernal, F. L. M.; Sottmann, J.; Wragg, D. S.; Fjellvåg, H.; Fjellvåg, Ø. S.; Drathen, C.; Slawinski, W. A.; Løvvik, O. M. Structural and Magnetic Characterization of the Elusive Jahn-Teller Active $NaCrF_3$. *Phys. Rev. Mater.* **2020**, *4*, No. 054412.
(21) Margadonna, S.; Karotsis, G. Cooperative Jahn-Teller Distortion, Phase Transitions, and Weak Ferromagnetism in the $KCrF_3$ Perovskite. *J. Am. Chem. Soc.* **2006**, *128*, 16436−16437.
(22) Fjellvåg, Ø. S.; Gonano, B.; Bernal, F. L. M.; Amedi, S. B.; Lyu, J.; Pomjakushin, V.; Medarde, M.; Chernyshov, D.; Marshall, K.; Valldor, M.; Fjellvåg, H.; Hauback, B. C. Order-to-Disorder Transition and Hydrogen Bonding in the Jahn−Teller Active NH_4CrF_3 Fluoroperovskite. *Inorg. Chem.* **2024**, *63*, 10594−10602.
(23) Ghazanfari, M. R.; Santhosh, A.; Siemensmeyer, K.; Fuß, F.; Staab, L.; Vrijmoed, J. C.; Peters, B.; Liesegang, M.; Dehnen, S.; Oeckler, O.; Jerabek, P.; Thiele, G. Large Exchange Bias, High Dielectric Constant, and Outstanding Ionic Conductivity in a Single-Phase Spin Glass. *Adv. Electron. Mater.* **2022**, *8*, 2200483.
(24) Jurca, T.; Farghal, A.; Lin, P.-H.; Korobkov, I.; Murugesu, M.; Richeson, D. S. Single-Molecule Magnet Behavior with a Single Metal Center Enhanced through Peripheral Ligand Modifications. *J. Am. Chem. Soc.* **2011**, *133*, 15814−15817.
(25) Liao, Q.; Kamerlin, S. C. L.; Strodel, B. Development and Application of a Nonbonded Cu^{2+} Model That Includes the Jahn−Teller Effect. *J. Phys. Chem. Lett.* **2015**, *6*, 2657−2662.
(26) Arčon, I.; Mirtič, B.; Kodre, A. Determination of Valence States of Chromium in Calcium Chromates by Using X-ray Absorption Near-Edge Structure (XANES) Spectroscopy. *J. Am. Ceram. Soc.* **1998**, *81*, 222−224.
(27) Mugiraneza, S.; Hallas, A. M. Tutorial: A Beginner's Guide to Interpreting Magnetic Susceptibility Data with the Curie-Weiss Law. *Commun. Phys.* **2022**, *5*, 95.
(28) Tezuka, K.; Shan, Y. J.; Imoto, H.; Ohoyama, K. Crystal and Magnetic Structures of Y_2CrS_4. *J. Phys. Chem. Solids* **2007**, *68*, 2133−2137.
(29) Liu, R. D.; Liu, Y. T.; He, L. H.; Wang, Z. C.; Chen, D. F.; Wang, F. W. The Crystal Structure, Magnetism, and Colossal Magnetoresistance of Y_2CrS_4. *Chin. Phys. B* **2012**, *21*, No. 057501.
(30) Mishra, P.; Sonia; Kumar, P. Effect of sintering temperature on dielectric, piezoelectric and ferroelectric properties of BZT−BCT 50/50 ceramics. *J. Alloys Compd.* **2012**, *545*, 210−215.
(31) Narendar, V. Performance Enhancement of FinFET Devices with Gate-Stack (GS) High-K Dielectrics for Nanoscale Applications. *Silicon.* **2018**, *10*, 2419−2429.
(32) Watt, G. W. Reactions of Inorganic Substances with Solutions of Metals in Liquid Ammonia. *Chem. Rev.* **1950**, *46*, 289−315.
(33) Dolomanov, O. V.; Bourhis, L. J.; Gildea, R. J.; Howard, J. A. K.; Puschmann, H. OLEX2: A Complete Structure Solution, Refinement and Analysis Program. *J. Appl. Crystallogr.* **2009**, *42*, 339−341.
(34) Sheldrick, G. M. SHELXT - Integrated Space-group and Crystal-structure Determination. *Acta Crystallogr. A* **2015**, *71*, 3−8.
(35) Sheldrick, G. M. Crystal Structure Refinement with SHELXL. *Acta Crystallogr. C* **2015**, *71*, 3−8.
(36) Brandenburg, K. *DIAMOND (4.6.4)*; Crystal Impact GbR: Bonn, 2020.
(37) Fuß, F.; Rieckert, M.; Steinhauer, S.; Liesegang, M.; Thiele, G. 3D-printed equipment to decouple (powder) X-ray diffraction sample preparation and measurement. *J. Appl. Crystallogr.* **2022**, *55*, 686−692.
(38) (a) Rietveld, H. M. Line Profiles of Neutron Powder-diffraction Peaks for Structure Refinement. *Acta Crystallogr.* **1967**, *22*, 151−152. (b) Rietveld, H. M. A Profile Refinement Method for Nuclear and Magnetic Structures. *J. Appl. Crystallogr.* **1969**, *2*, 65−71.

https://doi.org/10.1021/acs.chemmater.4c01764
Chem. Mater. 2024, 36, 9658−9665

(39) Toby, B. H.; von Dreele, R. B. GSAS-II: The Genesis of a Modern Open-source All Purpose Crystallography Software Package. *J. Appl. Crystallogr.* **2013**, *46*, 544−549.
(40) Többens, D. M.; Zander, S. KMC-2: An X-ray Beamline with Dedicated Diffraction and XAS Endstations at BESSY II. *J. Large Scale Res. Facil.* **2016**, *2*, A49.
(41) Ravel, B.; Newville, M. ATHENA, ARTEMIS, HEPHAESTUS: Data Analysis for X-ray Absorption Spectroscopy using IFEFFIT. *J. Synchrotron Radiat.* **2005**, *12*, 537−541.
(42) AMETEK Princeton Applied Research DataBase *Electrochemical Software*, 2022 https://www.ameteksi.com/library/application-notes/princeton-applied-research.
(43) Osman, Z.; Mohd Ghazali, M. I.; Othman, L.; Md Isa, K. B. AC Ionic Conductivity and DC Polarization Method of Lithium-ion Transport in PMMA−$LiBF_4$ Gel Polymer Electrolytes. *Results Phys.* **2012**, *2*, 1−4.

https://doi.org/10.1021/acs.chemmater.4c01764
Chem. Mater. 2024, 36, 9658−9665